CHEMISTRY OF SUPERCONDUCTOR MATERIALS

Preparation, Chemistry, Characterization and Theory

Edited by

Terrell A. Vanderah

Naval Weapons Center
China Lake, California

np NOYES PUBLICATIONS
Park Ridge, New Jersey, U.S.A.

Library of Congress Catalog Card Number: 90-27624
ISBN: 0-8155-1279-1
Printed in the United States

Published in the United States of America by
Noyes Publications
Mill Road, Park Ridge, New Jersey 07656

10 9 8 7 6 5 4 3 2 1

Library of Congress Cataloging-in-Publication Data

Chemistry of superconductor materials : preparation, chemistry, characterization and theory / edited by Terrell A. Vanderah.
p. cm.
Includes bibliographical references and index.
ISBN 0-8155-1279-1 :
1. Superconductors--Chemistry. I. Vanderah, Terrell A.
QC611.97.C54C48 1991
537.6'23--dc20 90-27624
CIP

For Jumbo Wells

89. Lee, M., Kapitulnik, A., and Beasley, M., Tunneling and the Energy Gap in High-Temperature Superconductors, *Mechanisms of High Temperature Superconductivity*, Eds. H. Kamimura and A. Oshiyama, Springer Series in Materials Science vol. 11, Springer-Verlag, Berlin (1989).

18

Static Magnetic Properties of High-Temperature Superconductors

Eugene L. Venturini

1.0 INTRODUCTION

The two fundamental physical properties of a superconducting material are zero electrical resistance and the Meissner effect (1) which is the expulsion of an externally applied magnetic field. The Meissner effect arises because the lowest energy state for the superconductor in weak external fields occurs when the internal magnetic induction B is zero (2)(3). The existence of the Meissner effect can be shown to prove that superconductivity is a stable thermodynamic equilibrium state (4). The expulsion of a field leads to unique magnetic properties of superconductors (5-7) which are the topic of this chapter. The chapter is divided into four main parts: the static response of superconductors to low magnetic fields, the response in relatively high fields, the relaxation of magnetization (flux creep), and the distinct features of porous ceramic superconductors.

Magnetic measurements have played a major role in the discovery and understanding of high-temperature superconductors, and an overwhelming body of literature has appeared in less than three years. In general, the magnetic properties of high-temperature superconductors were first understood for "conventional" superconductors, and several classic books are particularly useful. Appropriate papers on high-temperature superconductivity are cited, but not exhaustively, and there is no claim that a particular

reference is the first or even the "best" report concerning a given measurement.

There are four common instruments used to measure the magnetic response (moment) of a sample to an externally applied magnetic field, and each has strengths and weaknesses. Perhaps the most popular due to its sensitivity, ease of use and calibration, and accuracy is the **SQUID magnetometer** which employs an RF superconducting quantum interference device (SQUID) as the detector. The SQUID magnetometer measures the magnetic flux through a sense coil due to the sample magnetic moment. Also widely used is the **vibrating sample magnetometer** (VSM) which measures the changing dipolar field due to the magnetic moment of a vibrating sample. A third common instrument is the **Faraday balance** which determines the magnetic moment via the force exerted on a sample placed in a magnetic field gradient. The change in force (weight) is measured with a microbalance as a function of the average magnetic field strength. Finally, the **torque magnetometer** measures the torque on the sample when its magnetic moment is not aligned with an external magnetic field.

The VSM has the advantage of a fast response time and the ability to measure the sample moment in a continuously swept magnetic field. A minimum time constant of 1 second is typical for VSM studies of sample moments above 0.1 emu, and field sweeps are limited only by the inductance or power supply of the magnet. This fast response is particularly useful in studies of flux creep in superconductors (discussed below). In contrast, the SQUID magnetometer has the advantage of sensitivity: a moment of 10^{-6} emu is typically two orders of magnitude above the noise, allowing measurements on superconducting phases weighing a few micrograms distributed in a nonsuperconducting matrix weighing up to a few grams. However, the magnetic field must be stable to insure the sensitivity of a SQUID detector which limits the minimum response time to one or two minutes after a change in field strength. Hence, SQUID magnetometer data are obtained at discrete field values, although continuous temperature sweeps at a fixed field are possible. All data in this chapter were obtained with a commercial SQUID magnetometer (Biomagnetic Technologies, Inc., San Diego, CA, model VTS-905) with a temperature

range of 2 to 400 K and a magnetic field range of approximately 1 Oe to 50 kOe (10^{-4} to 5 Tesla). Although the technical journals strongly prefer the SI system of units, most books and research scientists continue to rely on the more convenient and practical Gaussian cgs units such as emu, Gauss (G) and Oersted (Oe) for magnetic measurements; these units are used throughout this chapter.

2.0 LOW-FIELD MEASUREMENTS

2.1 Normal State Response

Consider a long thin cylinder of superconducting material placed in a weak uniform magnetic field H as shown in Figure 1. Figure 1(a) illustrates the magnetic response of the cylinder in the normal state, i.e., at a temperature T above the superconducting transition temperature T_c. The magnetic field lines penetrate the cylinder, inducing a small magnetic moment m parallel to the field. In contrast, the magnetic field does not penetrate the cylinder when $T < T_c$ as shown in Figure 1(b) and discussed in the next subsection. The magnetization M is just this moment divided by the volume V of the cylinder, $M = m/V$. The moment m is commonly measured in emu and the volume in cm^3, leading to a magnetization in emu/cm^3 or Gauss (G). For most superconductors in the normal state, M (or m) is proportional to the internal magnetic field H_i:

$$M = m/V = \chi_v \cdot H_i \qquad (T > T_c) \qquad (1)$$

where the proportionality constant χ_v is termed the volume magnetic susceptibility and is dimensionless in the cgs system. Actually, there is a negligible difference between the external magnetic field H_e and the internal field H_i for nonmagnetic and nonsuperconducting solids, but the distinction is important for superconductors as discussed below. The magnetic induction B inside the sample is defined by:

$$B = H_i + 4\pi M = (1 + 4\pi\chi_v) \cdot H_i \qquad (2)$$

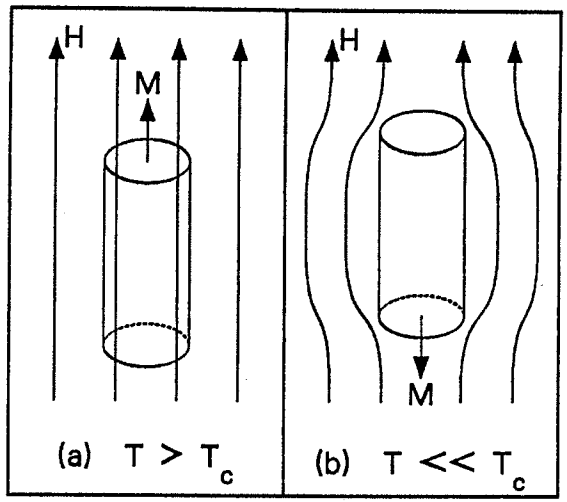

Figure 1: Magnetization M and magnetic field pattern for a long thin cylinder of material with a superconducting transition at temperature T_c placed in a small external field H: (a) at temperature $T > T_c$; (b) $T << T_c$.

Since it is much more convenient to weigh a sample than to measure its volume accurately, the magnetic response is often expressed as the moment per unit mass, m/W, where W is the weight of the cylinder. The proportionality between the internal field and the moment per unit mass is termed the mass magnetic susceptibility χ_g with units of cm^3/g. Obviously, χ_v and χ_g are simply related by the density of the cylinder $\rho = W/V$:

$$\chi_v = \rho \cdot \chi_g \tag{3}$$

It is useful to consider typical values of different contributions to the magnetic susceptibility. One important component is the Curie susceptibility arising from isolated (i.e., noninteracting) paramagnetic ions with g-factor g and spin S which is given by:

$$\chi = N \cdot (g \cdot \mu_B)^2 \cdot S \cdot (S+1)/(3 \cdot k_B \cdot T) \tag{4}$$

where N is the number of such ions, μ_B is the Bohr magneton, k_B is the Boltzmann constant, and T is the absolute temperature (8). The high-temperature superconductors contain Cu ions which are predominantly divalent. An isolated divalent Cu ion has a paramagnetic spin S = 1/2 and a g-factor g near 2, so Eq. 4 simplifies to:

$$\chi = (N/T) \cdot (\mu_B)^2/k_B = 6.230 \times 10^{-25} \cdot (N/T) \tag{5}$$

The superconducting material $YBa_2Cu_3O_7$ weighs 666 g/mole or 222 g/mole Cu. If all the Cu ions were divalent and acted as isolated spins, N in Eq. 4 would be 2.7×10^{21} Cu^{+2} ions per gram. Hence, the mass susceptibility χ_g would be 5.6×10^{-6} cm^3/g at room temperature (295 K) and would increase inversely with decreasing temperature, tripling to 1.7×10^{-5} cm^3/g at 100 K.

Another additive term in the magnetic susceptibility arises from the temperature-independent core diamagnetism of all the ions in a solid. For $YBa_2Cu_3O_7$ the core diamagnetism is approximately -2×10^{-7} based on a calculation using Pascal's constants (9). This small negative contribution serves to reduce the total susceptibility. A third possible contribution arises from Van Vleck paramagnetism (10) caused by excited states in the atoms of the

solid, while a fourth term is the band or Pauli paramagnetism minus the orbital diamagnetism (11) of the electrical carriers in the solid (holes in the case of $YBa_2Cu_3O_7$). Both the Van Vleck and Pauli contributions are positive and typically 10^{-5} to 10^{-6} cm^3/g, comparable to the Curie contribution above 100 K.

Finally, there is the question of interactions between the magnetic ions in the solid. There is a strong antiferromagnetic exchange coupling between the Cu ions in the CuO_2 sheets in high-temperature superconductors (actually superexchange coupling through the oxygen ions) (12). The insulating parent compounds such as La_2CuO_4 and $YBa_2Cu_3O_6$ exhibit long range antiferromagnetic ordering at temperatures near room temperature (12)(13). This ordering leads to a nearly temperature independent positive antiferromagnetic mass susceptibility below room temperature in the range of 10^{-7} to 10^{-6} cm^3/g from the Cu spins, in contrast to the inverse temperature dependence for a Curie susceptibility from Eq. 2. As carriers are added to the system, the correlation length for antiferromagnetic order decreases monotonically (as does the ordering temperature), and there is no long range antiferromagnetic order in the superconducting phase (14).

Typical normal state magnetic susceptibilities in the CuO-based high-temperature superconductors are nearly temperature independent above T_c and of order 10^{-6} cm^3/g. The values are not strongly affected by doping, remaining relatively constant from insulating antiferromagnetic La_2CuO_4 or $YBa_2Cu_3O_6$ with long range magnetic order to "metallic" $La_{1.85}Sr_{0.15}CuO_4$ or $YBa_2Cu_3O_7$ (15)(16). There is evidence from neutron scattering that the Cu ions continue to carry a spin in the metallic superconducting phase. The relative size of the various contributions to the magnetic susceptibility has not been firmly established for these systems, although estimates have been obtained for $La_{1-x}Sr_xCuO_4$ (17). However, it is clear that any strong positive increase in susceptibility with decreasing temperature reflects the presence of impurity phases with isolated paramagnetic Cu^{+2} ions, producing a Curie susceptibility. (Similarly, the detection of an electron paramagnetic resonance absorption near g = 2 indicates impurity phases containing isolated divalent Cu (18-20)).

2.2 Diamagnetic Shielding by a Superconductor

Diamagnetic **shielding** or flux **exclusion** is the response of a superconductor below T_c to a small applied magnetic field following zero-field cooling from above T_c. Figure 1(b) illustrates the situation for a superconducting cylinder in a small field H at a temperature well below T_c. The lowest energy state has the magnetic induction B equal to zero in the interior of the cylinder. Screening (shielding) supercurrents flow in the near surface region of the cylinder to exactly cancel the applied field in the interior, and the cylinder appears to have a large negative moment. The field relationship inside may be written as (21):

$$B = H_i + 4\pi M = 0 \qquad (6)$$

Hence $4\pi M = -H_i$, and the volume susceptibility for a long thin superconducting cylinder with its axis oriented parallel to the applied field is given by:

$$\chi_v = M/H_i = m/(V \cdot H_i) = -1/4\pi \qquad (7)$$

The shielding fraction is a comparison between the measured volume susceptibility and $-1/4\pi$, and it is given simply by $-4\pi\chi_v = -4\pi\rho\chi_g$.

There are several details which complicate this simple picture. All high temperature superconductors are type II superconductors, and they have a lower critical field strength H_{c1} above which the shielding is no longer complete. This is illustrated schematically in Figure 2 which shows the magnetization M versus increasing field H_i. The solid line indicates the response of a "perfect" type II superconductor. M increases linearly with H_i (slope = $\chi_v = -1/4\pi$ from Eq. 7) when $H_i < H_{c1}$. There is a cusp at H_{c1}, above which the magnetic induction B is no longer zero in the lowest energy state, and magnetic flux enters the superconductor. When H_i reaches the upper critical field strength H_{c2}, the superconducting order parameter is zero, and the material acts as a normal metal for $H_i > H_{c2}$. For $H_{c1} < H_i < H_{c2}$ the flux in the superconductor is less than that in the normal state, and the material is said to be in the mixed state.

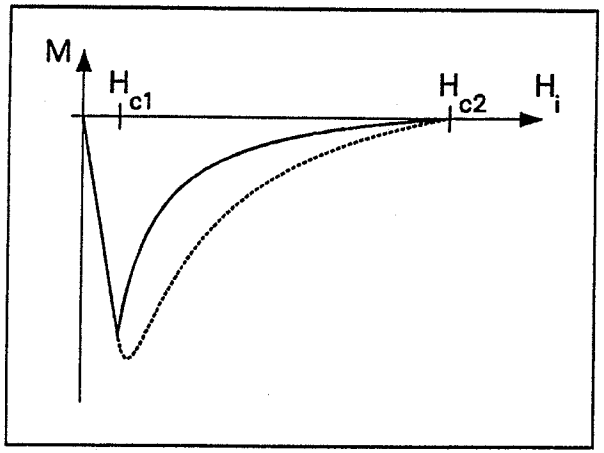

Figure 2: Shielding magnetization M versus increasing internal field H_i for a type II superconductor. The solid line shows the "ideal" response (i.e., with no flux pinning) with a cusp at the lower critical field H_{c1}; the dashed line shows the changes due to pinning. The material is superconducting for H_i below the upper critical field H_{c2} and a normal metal at higher fields.

There are two characteristic length scales in superconductors, the coherence length ξ and the penetration depth λ. The superconducting ground state is characterized by an order parameter which exhibits coherence over a spatial distance ξ, the coherence length for the paired carriers. The internal magnetic field H_i and supercurrent J_s vary over a characteristic distance λ, the penetration depth. For most type II superconductors including the high-T_c materials, $\lambda >> \xi$. When a type II superconductor is in the mixed state, the flux appears as quantized units termed magnetic vortices, flux lines, or simply fluxoids. Each fluxoid contains one flux quantum $\phi_o = hc/2e = 2.07 \times 10^{-7}$ G·cm^2 where h is Planck's constant, c is the speed of light in vacuum, and e is the electron charge. A fluxoid consists of a cylindrical core where the superconducting order parameter rises from zero to its full value over a coherence length ξ. This core is surrounded by a cylinder of supercurrents flowing in a circular vortex pattern throughout a thickness equal to the penetration depth λ, generating a quantum of flux ϕ_o (22).

These flux lines are "pinned" at internal defects and by surface imperfections in all type II superconductors, leading to the magnetic response shown by the dashed line in Figure 2. Pinning has no effect when $H_i < H_{c1}$, since there is no flux entering the bulk of the superconductor (see below). However, the linear M-H curve has no cusp at H_{c1} when pinning is present; rather, there is a gradual deviation from linearity as flux lines overcome surface pinning and internal defect pinning to penetrate the superconductor. Finally, the magnetization reaches a minimum determined by the strength of the pinning and decreases for higher fields. Note that pinning has no effect on the value of H_{c2}, although the shape of the M-H curve in the mixed state is affected. Flux lines are not independent, and under appropriate conditions they can interact to form a flux lattice (Abrikosov lattice (22)) which exhibits collective pinning. The effects of this lattice are beyond the scope of this chapter.

When $H_i < H_{c1}$, B = 0 in the interior of the superconducting cylinder as shown in Figure 1(b), but magnetic flux enters the walls for a distance λ ($\approx$1400 Å for fields parallel to the a-b plane in $YBa_2Cu_3O_7$ at low temperatures (23)). Provided the sample is of macroscopic size, the penetration depth is negligible, but it

becomes important for fine powders, fine-grained ceramics, and thin crystal plates. Two equations are useful for determining the correction for the penetration depth. First, the penetration depth is nearly temperature independent except when T approaches T_c (24):

$$\lambda(T) = \lambda(T=0)\cdot\{1 - (T/T_c)^4\}^{-1/2} \quad (8)$$

For a field applied parallel to the broad face of a thin rectangular plate of thickness d, the penetration depth reduces the shielding susceptibility by (25):

$$\chi/\chi_o = 1 - \{(2\cdot\lambda)/d\}\cdot\tanh\{d/(2\cdot\lambda)\} \quad (9)$$

where χ_o is the susceptibility when the penetration depth is negligible. Similar correction formulas for fine powder samples are available (26).

Another complication is the demagnetization correction due to the geometry of the specimen. Demagnetization (or the equivalent depolarization problem for dielectric bodies in an electric field) can only be solved analytically for an ellipsoid of revolution (27)(28). When H_e is applied parallel to one of the three axes of revolution, the magnetization is parallel to H_e, but the internal field H_i is given by (29):

$$H_i = H_e - 4\pi DM \quad (10)$$

where D is termed the demagnetization factor. Substituting this relation for H_i in Eq. 7 and solving for M, we can define an experimental susceptibility χ_e relating M to the external magnetic field H_e:

$$\chi_e = M/H_e = \chi_v/(1 + 4\pi D\cdot\chi_v) = -1/\{4\pi\cdot(1 - D)\} \quad (11)$$

Since D is between 0 and 1 in all cases and $\chi_v < 0$, demagnetization produces an enhanced experimental susceptibility compared to the true volume susceptibility.

Some common shapes have the following demagnetization factors (30). D = 0 for fields applied parallel to an infinite sheet

and D = 1 for fields normal to the sheet (i.e., χ_e becomes infinite). D = 1/2 for fields applied normal to the axis of an infinite cylinder and D = 0 for fields parallel to the axis (hence the choice of a "long thin" cylinder parallel to H in Figure 1). Finally, D = 1/3 for fields in any direction if the sample is a sphere. Measurements with the applied field normal to a thin crystal or a thin film must be corrected for demagnetization which can be very large. For example, the measured low-field susceptibility was $-4750/4\pi$ with the field normal to a 0.3 μm-thick $Tl_2Ca_2Ba_2Cu_3O_x$ film with a 3x3 mm^2 cross-section (31).

An example of a diamagnetic shielding or flux exclusion measurement is shown in Figure 3 where we plot the magnetization versus external field strength at 5 K for a thin crystal of $YBa_2Cu_3O_{7-\delta}$. This crystal has dimensions 1.10 x 0.62 x 0.040 mm^3, and the data were taken with the field applied parallel to the longest dimension. The demagnetization factor D is approximately 0.02 for this geometry, so complete diamagnetic shielding would be reflected in an experimental susceptibility $\chi_e = -1.02/4\pi$ from Eq. 11 compared to the measured value of $-0.96/4\pi$; hence the shielding fraction is 0.94. There is a slight correction for the penetration depth λ which is 1400 Å for fields parallel to the a-b plane of $YBa_2Cu_3O_{7-\delta}$: using the thickness d = 40 μm in Eq. 9, we obtain $\chi/\chi_o = 0.993$. Hence, the finite penetration depth reduces the susceptibility for complete diamagnetic shielding by nearly 1%, effectively raising the measured shielding fraction to 0.95. Clearly, as T approaches T_c and λ increases dramatically according to Eq. 8, the measured shielding susceptibility will fall rapidly. This decrease in χ with increasing temperature provides a direct measurement (23) of $\lambda(T)$ using Eq. 9, provided H_i remains below H_{c1} at all temperatures.

The data in Figure 3 also provide a determination of the lower critical field H_{c1}. The shielding response will remain linear in the applied field until flux lines start to enter the crystal. Assuming a negligible surface barrier to flux penetration, H_{c1} is determined by the point where the M-H curve deviates from linearity. In Figure 3 this occurs between 280 and 300 Oe, in good agreement with a recent estimate of 250±50 Oe from magnetic relaxation (32), but somewhat higher than estimates of 120(10) Oe obtained by the same method of deviation from

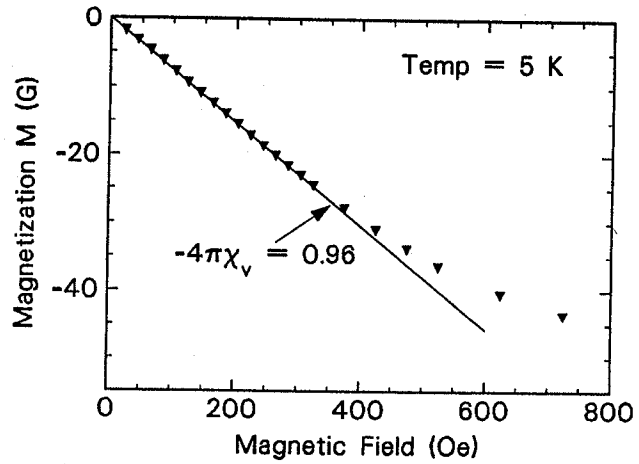

Figure 3: Shielding magnetization at 5 K versus increasing external field for a superconducting $YBa_2Cu_3O_{7-\delta}$ single crystal.

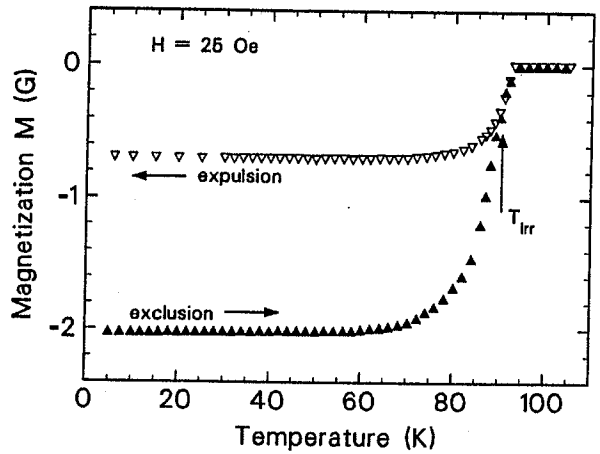

Figure 4: Flux exclusion (shielding) versus increasing temperature (solid triangles) and flux expulsion (Meissner effect) versus decreasing temperature (open triangles) in a 25 Oe external field for a superconducting $YBa_2Cu_3O_{7-\delta}$ single crystal. Exclusion and expulsion are equal for temperatures above the irreversibility point T_{irr} (≈90.5 K at 25 Oe); T_c is 92 K.

linearity in the M-H curve (33) and 180(20) Oe obtained from flux exclusion versus temperature (34).

2.3 Magnetic Flux Exclusion and Expulsion

Diamagnetic shielding is measured by applying a small magnetic field after cooling the superconductor below T_c in nearly zero field. This effect is also termed flux exclusion since the superconductor supports screening currents near the surface to exclude the magnetic flux associated with the applied field. In contrast, one can apply the external field at a temperature T above T_c and measure the magnetization as the sample cools. In sufficiently small fields ($H_i < H_{c1}(T)$), the lowest energy state of the superconductor has B = 0, and the sample achieves this state by expelling the magnetic flux associated with the external field. This flux **expulsion** is termed the Meissner effect after its discovery by Meissner and Ochsenfeld in 1933 (1) (it should be called the Meissner-Ochsenfeld effect).

Figure 4 compares the flux exclusion and flux expulsion versus temperature measured in a field of 25 Oe applied parallel to the long axis of the same single crystal of $YBa_2Cu_3O_{7-\delta}$ discussed above. For temperatures above T_c = 92 K the magnetization is slightly positive (≈ 6 x 10^{-5} G), but becomes large and negative at lower temperatures for both expulsion and exclusion measurements. This is one of the simplest tests for superconductivity: an abrupt decrease in the measured susceptibility. Typically, a SQUID magnetometer can easily detect a superconducting volume fraction of 0.001% since χ_v is $-1/4\pi$ compared to a normal state χ_v of 10^{-6} or less. The rapid decrease in exclusion with increasing temperature beginning near 75 K in Figure 4 occurs because H_i exceeds $H_{c1}(T)$. Flux lines enter the superconducting crystal, and the magnetization decreases. This offers another method to determine $H_{c1}(T)$ by measuring exclusion versus temperature as a function of magnetic field (34).

Note that the expulsion and exclusion responses are equal for T close to T_c. This "reversible" region extends from T_c down to an "irreversibility" temperature T_{irr} which is a function of the applied field, varying as $(H_e)^{2/3}$ (35). The lack of reversibility at temperatures below T_{irr} indicates pinning of the magnetic flux: the

Meissner state requires that the sample expel the flux as it cools, and this cannot occur if the flux lines are pinned by impurities, defects or perhaps an intrinsic pinning mechanism (36). If there were no flux pinning, the exclusion and expulsion data would overlap at all temperatures. Hence, T_{irr} is that temperature below which the flux expulsion does not reach a true equilibrium Meissner state. If the field is removed following field cooling to a temperature $T < T_{irr}$, the sample exhibits a "remanent moment" opposite in sign to the Meissner signal. In fact, this moment equals the difference between the exclusion and expulsion curves at temperature T (see Figure 4). This equality demonstrates the importance of flux pinning in understanding magnetization data of high-temperature superconductors (37).

In the previous section we defined the shielding fraction as the ratio of the measured volume susceptibility following zero field cooling to the complete shielding value of $-1/4\pi$ (neglecting the finite penetration depth and including a correction for demagnetization). In a similar fashion, we can define a Meissner fraction as the ratio of the measured volume susceptibility to $-1/4\pi$ following field cooling. The shielding fraction will always be greater than the Meissner fraction for temperatures below T_{irr} where flux pinning occurs. Why is this important? Consider the situation where the superconducting portion of the sample is a relatively thick "shell" on a nonsuperconducting interior (38)(39). Provided that the shell thickness is large compared to the penetration depth λ, the flux will be excluded from the entire body by screening currents in the shell. Hence the shielding fraction will approach unity, indistinguishable from the situation where the entire sample is superconducting. In contrast, the nonsuperconducting interior will not expel the flux in a Meissner measurement, and only the superconducting shell will produce a Meissner signal. Hence, the Meissner fraction provides a reliable lower estimate on the "true" superconducting fraction (with the same caveats about penetration depth and demagnetization correction as in the shielding fraction).

If the entire body is superconducting, the Meissner fraction will be reduced due to flux pinning (40). How can one determine whether a low Meissner fraction is due to flux pinning and/or due to a sample problem like superconducting "shells"? One approach

is to measure both the shielding and Meissner fractions as a function of applied field. If the two fractions agree at low temperature, the entire sample must be superconducting. There is always a reversible region sufficiently close to T_c where a true equilibrium Meissner state is achieved (i.e., where exclusion and expulsion are equivalent). If $H_{c1}(T)$ exceeds H_i during cooling in the reversible region, the sample will achieve a true Meissner state, and the exclusion and expulsion will remain in complete agreement at all lower temperatures. The experimental difficulty is choosing a sufficiently small measurement field to satisfy this criterion.

Our approach has been to measure both exclusion and expulsion at a low temperature (typically 10 K for $YBa_2Cu_3O_{7-\delta}$) and plot the ratio versus applied field. Figure 5 shows exclusion and expulsion measurements at 10 K versus applied fields from 2.5 to 700 Oe. The Meissner data are nearly independent of field above approximately 60 Oe, suggesting that the trapped flux is strongly pinned at higher fields when T decreases through T_{irr}. This also means that the Meissner fraction will be anomalously low if the measurement field is "too large". The shielding data are linear in field to approximately 300 Oe as previously shown in Figure 3 (a different crystal was used for the data in Figure 5). However, the shielding magnetization saturates near 600 Oe in Figure 5, while it is still increasing at 725 Oe in Figure 3. This implies that the crystal used for Figure 5 has less flux pinning at 10 K than that used for Figure 3. The onset of nonlinear behavior in the M-H exclusion curve indicates that the internal field H_i has reached H_{c1} at that temperature. Stronger fields place the sample in the mixed state, and pinning will prevent the flux from entering the sample freely. More pinning will result in a higher shielding magnetization at a given $H_i > H_{c1}$ due to less complete flux penetration.

Figure 6 shows the exclusion/expulsion ratio versus applied field using the data from Figure 5. The inset to Figure 6 emphasizes the behavior at low fields: as the measurement field is reduced below 10 Oe, the exclusion/expulsion ratio decreases smoothly to unity. This confirms that the entire crystal is superconducting, since the shielding fraction for this crystal is approximately 0.97 from the linear portion of the shielding M-H curve. There is a decided advantage to plotting the exclu-

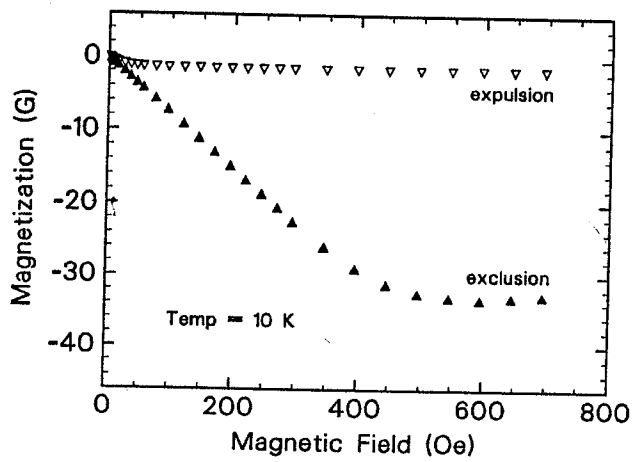

Figure 5: Flux exclusion and flux expulsion at 10 K versus external magnetic field for a superconducting $YBa_2Cu_3O_{7-\delta}$ single crystal.

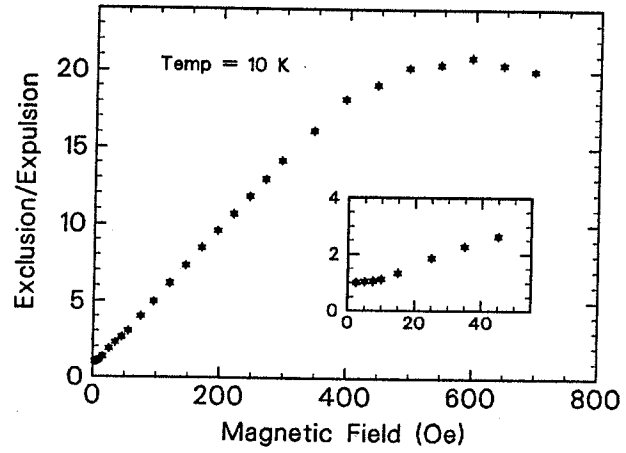

Figure 6: Ratio of flux exclusion to flux expulsion at 10 K versus external magnetic field for a superconducting $YBa_2Cu_3O_{7-\delta}$ single crystal. The inset shows that this ratio approaches unity at very low fields.

sion/expulsion ratio as in Figure 6: the complications due to demagnetization and penetration depth are removed since they enter both exclusion and expulsion equally in the limit of no pinning. Hence a ratio of unity implies complete superconductivity, provided that the shielding fraction is unity.

3.0 HIGH-FIELD MEASUREMENTS: HYSTERESIS LOOPS AND CRITICAL CURRENT DENSITY

Magnetization measurements at high magnetic fields $H_e >> H_{c1}$ can be used to study flux pinning and to extract a magnetization critical current density J_{cm}. Figure 7 illustrates schematically a complete isothermal hysteresis loop for a typical type II superconductor with strong flux pinning (41). The dashed line shows the initial shielding response versus increasing field following cooling to the measurement temperature in zero field. At the highest field to the right of Figure 7 the sample is well into the mixed state, and the shielding current is uniform and equal to the critical current density throughout the sample. If the field sweep is then reversed, there is a rapid reversal of the shielding current near the surface, while the flux which entered during the increasing field cycle remains pinned within the sample. This results in a positive external magnetization (i.e., parallel to the external field) and a substantial hysteresis (difference) between M for increasing and decreasing fields. As the decreasing field sweep crosses zero and approaches a maximum in the opposite direction, the shielding currents again become uniform at the critical current density, but in the reverse sense. Hence, as the sweep direction is reversed again at the far left in Figure 7, the magnetization reverses sign and hysteresis is observed. Note that after the initial increasing field sweep (dashed line), the magnetization is reasonably symmetric about zero field, and the curve shown as a solid line can be retraced indefinitely.

For H_e much larger than H_{c1} the magnetization in Figure 7 is nearly the same on the initial (dashed) and repetitive (solid) curves for a given increasing field value. Hence one can accurately determine the hysteresis ΔM for "large" fields using only a partial loop where the field is increased from zero to a maximum

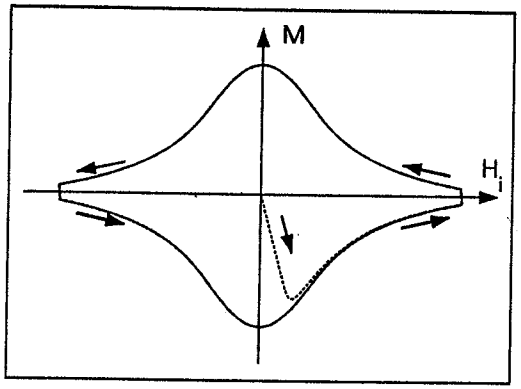

Figure 7: Sketch of a complete magnetization hysteresis loop versus internal magnetic field H_i. The dashed line is the initial response following zero field cooling, while the solid line is the response for repeated cycles between maximum and minimum field strengths. The arrows indicate the direction of the field sweep, and the hysteresis is the difference in magnetization at a given field during increasing and decreasing field sweeps.

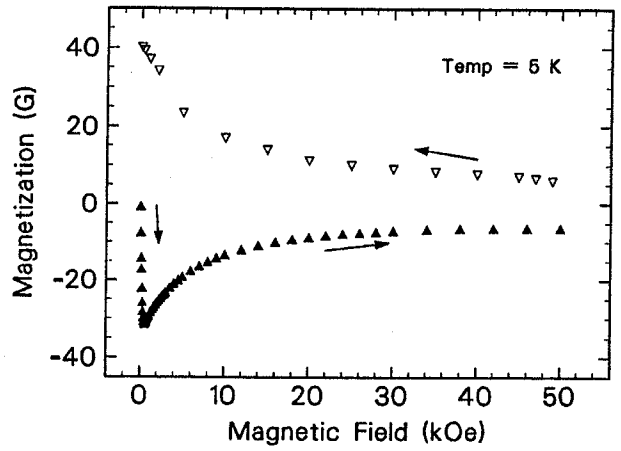

Figure 8: Partial magnetization hysteresis loop at 5 K for a superconducting $YBa_2Cu_3O_{7-\delta}$ single crystal. The solid triangles represent the response to increasing fields while the open triangles are for decreasing fields.

value and then decreased back to zero. Figure 8 shows such a partial hysteresis loop measured at 5 K with the magnetic field applied along the long axis of the same $YBa_2Cu_3O_{7-\delta}$ single crystal used for Figure 3. The arrows indicate the field change direction beginning near zero field; increasing field data are shown as solid triangles, while open triangles represent decreasing fields. The large negative magnetization due to the shielding supercurrents reaches a minimum near 800 Oe as flux lines penetrate the crystal. As the field strength increases to 50 kOe, the magnetization decreases as more flux enters the crystal and the critical current density decreases in the stronger field. As the field is decreased below 50 kOe, the magnetization reverses direction rapidly to a positive value nearly equal in magnitude to the negative magnetization recorded at the highest increasing field.

This behavior reflects strong pinning of the flux lines in the crystal at 5 K and is explained by the Bean critical state model for hard (strongly pinned) type II superconductors (42-47). In fact, the hysteresis in magnetization $\Delta M = M(H_e^-) - M(H_e^+)$, where H_e^- denotes decreasing field and H_e^+ denotes increasing field, is proportional to the critical current density J_{cm} flowing in the sample (the subscript "m" is used to distinguish this result from the critical current density measured by direct transport and denoted J_{ct}). Two common geometries for magnetization field-loop (hysteresis) measurements are with the field applied parallel to the axis of a cylinder (or thin disk) of diameter d or normal to one face of a rectangular slab with cross-section axb. In the case of the cylinder:

$$J_{cm} = 30 \cdot \Delta M/d, \tag{12}$$

while for the rectangular slab with a > b:

$$J_{cm} = (20 \cdot \Delta M/b)/(1 - b/3a). \tag{13}$$

We obtain $\Delta M(H_e)$ from the data in Figure 8 and calculate $J_{cm}(H_e)$ using the rectangular slab Eq. 13 where a = 0.62 mm and b = 0.040 mm. The result is shown in Figure 9 where the magnetization critical current density J_{cm} falls monotonically with increasing field strength. Actually, Eq. 13 must be modified for

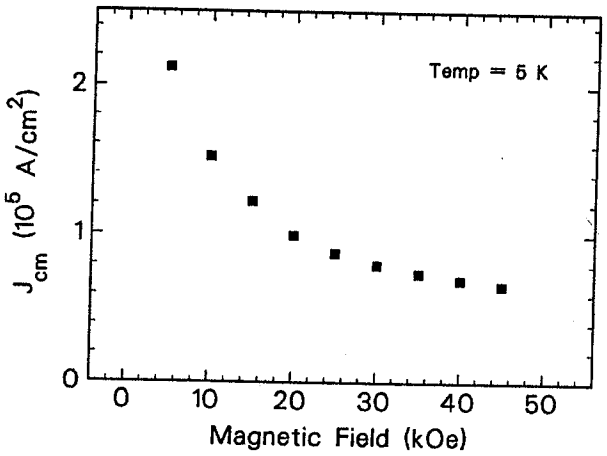

Figure 9: Magnetization critical current density J_{cm} at 5 K versus external magnetic field calculated from the hysteresis loop data in Figure 8 using the Bean critical state model [42].

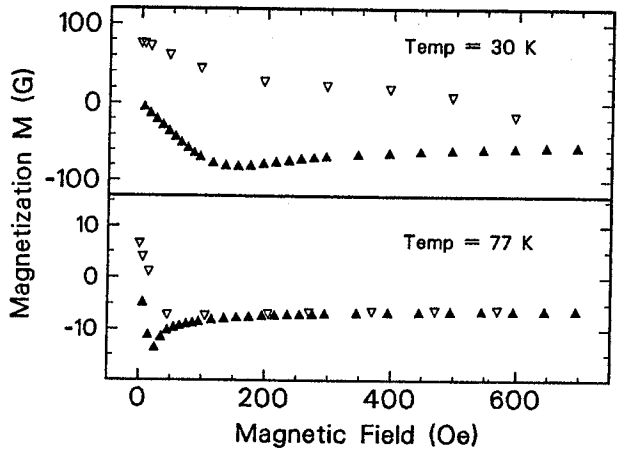

Figure 10: Comparison of partial magnetization hysteresis loops at 30 and 77 K for a superconducting $Tl_2Ca_1Ba_2Cu_2O_8$ single crystal (T_c is 105 K). The lack of hysteresis at 77 K is due to weak flux pinning.

the case of anisotropic critical current observed in all the high-temperature superconductors (48). J_{cm} in Figure 9 reflects critical current flowing along the c axis of the $YBa_2Cu_3O_{7-\delta}$ crystal and is in good agreement with similar measurements on other crystals (48-50).

Certain conditions must be satisfied for Eqs. 12 and 13 to be valid: (1) the applied field H_e must be large compared to H_{c1}, (2) the field variation across the sample must be small, and (3) the maximum field in the loop must be large enough to insure that critical currents are induced in the same sense throughout the sample (51). Condition (3) can be expressed as a minimum field strength H_p for complete penetration of critical current to the center of the sample (41,52). The situation for H_e comparable to or less than H_{c1} is considerably more complicated (53). Condition (2) is not satisfied when the flux lines are weakly pinned. Weak pinning combined with high temperatures in the copper-oxide based superconductors leads to "giant flux creep" (54) which is the subject of the next section.

Figure 10 shows the dramatic effects of weak pinning by comparing isothermal hysteresis loops at 30 and 77K in a $Tl_2Ca_1Ba_2Cu_2O_8$ single crystal. These data were recorded with the field applied along the crystal c axis (normal to the large surface), and the solid triangles represent increasing field strength while the open triangles show decreasing fields. The hysteresis loop at 30 K is relatively open, suggesting reasonably strong flux pinning (the hysteresis persists to 10 kOe). Conditions (1) to (3) above are satisfied, and we can use Eq. 13 to estimate $J_{cm} \approx 5.3X10^4$ A/cm^2 at 30 K in 400 Oe. In contrast, there is virtually no hysteresis above 200 Oe at 77 K for this same crystal (note the change in vertical scale). The negative magnetization and lack of hysteresis suggests reversible flux concentrations, the opposite of strong pinning. The thermal energy at 77 K results in easy flux motion (see below), and condition (2) above is not satisfied. Hence the Bean model is not applicable, and Eqs. 12 or 13 cannot be used to obtain J_{cm}. Small hysteresis has also been reported for $YBa_2Cu_3O_{7-\delta}$ (50,55-57), $Bi_2Sr_2CaCu_2O_8$ (58-60) and $Tl_2Ca_2Ba_2Cu_3O_{10}$ (61)(62).

The comparison of critical current density obtained from direct transport measurements (termed J_{ct}) with that inferred from

magnetization hysteresis data J_{cm} is controversial when the flux pinning is weak, i.e., at high temperatures in $YBa_2Cu_3O_{7-\delta}$ or moderate temperatures in the Bi-Sr-Ca-Cu-O and Tl-Ca-Ba-Cu-O superconductors (58)(61)(63-68). J_{ct} from a pulsed measurement can exceed J_{cm} from hysteresis by two orders of magnitude when flux motion is rapid (58)(61), but J_{cm} from the critical state model (Eq. 12) may not be valid when pinning is weak. The agreement is considerably better at low temperatures where flux motion is limited (58)(61)(68). A further complication in this comparison is caused by the different time scales of the two experiments: magnetization data in a SQUID magnetometer are recorded over minutes (isothermal hysteresis loops with 50 points typically require 8 hours), while transport data are frequently obtained using submillisecond pulses to minimize sample heating at the current contacts (58)(61)(63). In fact, the amount of hysteresis can depend on the rate of field sweep (64), and vibrating sample magnetometers have a decided advantage over SQUID magnetometers in this situation. Since flux creep is a dynamic process, J_{ct} and J_{cm} must be measured on the same time scale for a realistic comparison.

4.0 MAGNETIZATION RELAXATION OR GIANT FLUX CREEP

Thermally activated flux motion or creep has been studied extensively in conventional type II metallic superconductors (69-74). This motion is governed by the thermal energy relative to the average flux pinning energy. The thermal energy is higher in high-T_c superconductors because of the higher possible measurement temperatures, while the pinning energy is considerably smaller due to the short coherence lengths (54). Hence, flux moves easily in high-T_c materials (75-77) compared to conventional superconductors, leading to the phenomenon termed "giant flux creep" (54) where the magnetization changes by a large fraction on a time scale of minutes. An alternate interpretation of magnetization relaxation in terms of a superconducting "glass" state has been proposed (75)(78).

The basic measurement of flux creep is magnetization versus time (relaxation) in a constant field at fixed temperature (73). The

magnetization changes as flux lines move into or out of a superconductor. Inward flux creep in the mixed state is studied by stabilizing the sample at a fixed temperature at one field strength (typically zero field) and then applying a stronger field $H_e > H_{c1}$. Flux motion into the sample is reflected by the decrease in magnetization with time as it relaxes toward the equilibrium Meissner state for that field and temperature. Outward flux creep is analogous: the sample is stabilized at the measurement temperature in a high field $H_e > H_{c1}$, the field is changed to a lower value (typically zero field), and the magnetization relaxes with time toward the equilibrium Meissner state (which is zero magnetization for zero field).

Typical magnetization relaxation data (65) at 10 K are shown in Figure 11 with the external magnetic field applied normal to a 0.7 μm-thick $Tl_2Ca_2Ba_2Cu_3O_{10}$ (Tl-2223) film on $SrTiO_3$. The solid triangles reflect flux motion out of the film following a step change from 10 kOe to nearly zero field. The open triangles show flux creep into the film after a step change from nearly zero field to 500 Oe. These situations are quite different: for flux creep out of the film, the measured signal reflects critical current flow at nearly zero field arising from pinned flux remaining after a field sweep from the mixed state to zero field (top data in Figure 11). An important point is the history of the mixed state preparation: we have found that consistent results are obtained if the large field (10 kOe for this case) is applied at an elevated temperature (> 50 K for Tl-2223) where flux motion is rapid and a near equilibrium state is achieved quickly (as shown by the absence of hysteresis). Then the sample can be cooled to the measurement temperature prior to lowering the field strength. For flux creep into the film, the shielding response reflects critical current flow to exclude the applied field (bottom data in Figure 11). Clearly, the flux motion is similar in these two physically distinct measurements.

The semi-log plot in Figure 11 emphasizes the logarithmic time dependence of the magnetization signal for times between 200 and 4000 seconds. These data are consistent with thermally activated flux motion (54)(63)(65)(69-74)(79-86). The data for flux motion out of the film were extended to 7500 seconds with no observed change in behavior. Similar relaxation data (76) for $La_{1.8}Sr_{0.2}CuO_4$ ceramic showed logarithmic time dependence over

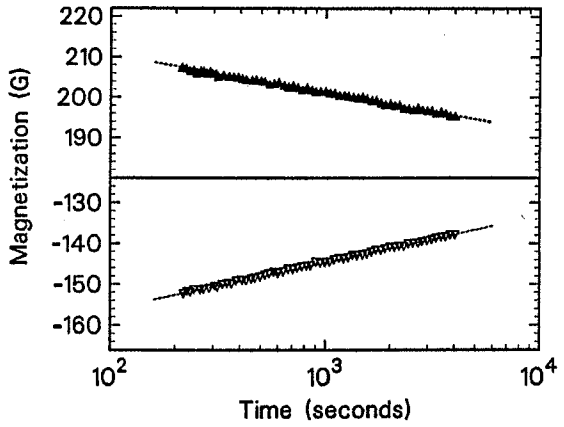

Figure 11: Magnetization relaxation versus log(time) at 10 K in fields applied normal to a 0.7 μm-thick $Tl_2Ca_2Ba_2Cu_3O_{10}$ superconducting film (T_c is 108 K). The solid triangles show relaxation due to flux creep out of the film in zero applied field after cooling in a 10 kOe field and removal of the field. The open triangles represent flux creep into the film in a 500 Oe field applied following zero field cooling. The dashed lines show the fit to Eq. (13).

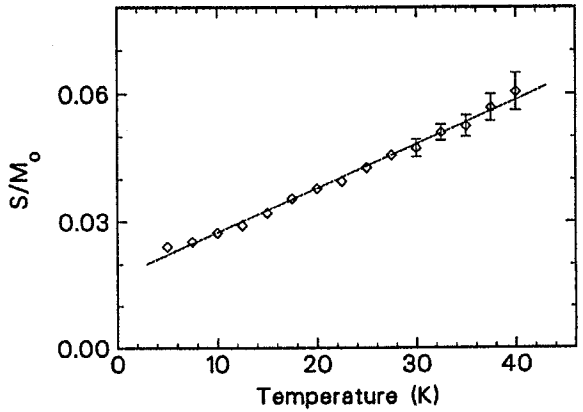

Figure 12: Ratio of flux creep rate S(T) to the magnetization at 1 second $M_o(T)$ versus temperature. S and M_o are obtained by fitting data such as those in Figure 11 using Eq. (13). The slope of the dashed line corresponds to an effective flux pinning potential U = 83 meV according to a simple thermally activated flux creep model which yields Eq. (14).

four decades from 10 seconds to 24 hours. The zero of time for the magnetization data in Figure 11 is defined as the time when the field sweep in our SQUID susceptometer reaches the measurement field. Due to the design of this instrument, there is a dead time of approximately 200 seconds after the field sweep stops before useful data can be recorded.

The dashed lines in Figure 11 represent a simple two-parameter linear fit to the logarithmic time dependence:

$$M(t,T) - M_{eq}(T) = M_o(T) + S(T)\cdot\ln(t) \qquad (14)$$

where M(t,T) is the magnetization at time t and temperature T, $M_{eq}(T)$ is the equilibrium magnetization for the Meissner state at the measurement field and temperature (M_{eq} is zero for flux creep out of the sample when the measurement field is zero), $M_o(T)$ is the extrapolated magnetization at t = 1 second, and S(T) = $d(M(t,T)-M_{eq}(T))/d\ln(t)$ is the creep rate (63)(73)(83-85). Measurements at temperatures between 5 and 40 K for flux creep into the film in 500 Oe show a similar logarithmic time dependence. The simple time dependence in Eq. 14 is valid over a limited range of field, temperature and time in an activated flux creep model (63)(73)(83-85), and we have frequently observed strong deviations experimentally at both short and long times, particularly for single crystals.

The two fitting parameters in Eq. 14 can be used to extract an average pinning potential U by fitting the magnetization time dependence for data taken over a range of temperatures (83-85):

$$S(T)/M_o(T) = k_BT/U \qquad (15)$$

where k_B is the Boltzmann constant. Figure 12 plots this ratio $S(T)/M_o(T)$ for flux creep out of the film versus temperature, demonstrating the linear relation given by Eq. 15. The dashed line corresponds to U = 83 meV (65), which is a rather small pinning potential. This weak flux pinning with activated motion explains the hysteresis collapse at 77 K shown in Figure 10. Considerably more detailed treatments of magnetization relaxation than Eq. 15 have been published (63)(81)(84)(85).

Eq. 15 predicts no flux creep at T=0 (no thermal energy),

while the data in Figure 12 do not extrapolate to zero at T=0. This suggests that the creep in these films may be driven by mechanisms more complex than simple thermal activation including a distribution of activation energies (63). Other $Tl_2Ca_2Ba_2Cu_3O_{10}$ films with higher transport critical current densities show somewhat lower pinning potentials between 50 and 60 meV. In contrast, magnetization relaxation measurements on a $Tl_2Ca_2Ba_2Cu_3O_{10}$ single crystal with the field applied along the c axis (normal to the broad face) show a pinning potential of only 15 meV, consistent with the weak pinning in $Bi_2Sr_2CaCu_2O_8$ (60)(80). It is clear that grain boundary pinning has an important influence on flux motion and transport critical currents in granular thin films or bulk ceramics, and the pinning strength will differ at grain boundaries and within individual grains. Further, the presence of impurity phases can also dramatically alter the magnetization hysteresis and flux pinning.

5.0 PROBLEMS WITH POROUS AND WEAK-LINKED CERAMICS

A final topic in magnetization studies of high-temperature superconductors is the problem of ceramic samples where porosity and the presence of both **intergranular** and **intragranular** supercurrents complicate the analysis. Soon after the discovery (87)(88) of copper-oxide-based high-temperature superconductors, transport measurements (89) on ceramic samples showed a dramatic drop in critical current in the presence of very modest magnetic fields. This behavior was attributed to weak links acting as Josephson junctions between grains, leading to a two order of magnitude drop in J_{ct} between zero field and 100 Oe. A similar decrease occurs in the intergranular magnetization shielding supercurrents (90)(91) which has been termed "grain decoupling" (90) at low magnetic fields. The effects of granularity on critical current density and magnetization have been treated theoretically (92).

Typical shielding data at 5 K versus low field are shown in Figure 13 for a sintered, oxygen-annealed $YBa_2Cu_3O_{7-\delta}$ bulk ceramic plate cut to a rectangular plate of dimensions 8 x 6 x 0.7mm^3. Preparation conditions are given elsewhere (90). The plate

was oriented with the long direction parallel to the applied field to minimize demagnetization effects. The shielding response is linear in field below about 20 Oe (dashed line) with a slope $\chi_e = -1.02/4\pi$, exhibits a nonlinear field dependence between 20 and 60 Oe, and becomes linear again between 60 and 200 Oe (solid line) with a slope $\chi_e = -0.69/4\pi$.

Consider first the linear response at very low field. The demagnetization factor with the field along the longest dimension is $D \approx 0.05$ (27), so from Eq. 11 we obtain a volume susceptibility $\chi_v = (1-D)\cdot\chi_e = -0.97/4\pi$. Hence the shielding fraction is 97%, corresponding to nearly complete screening from the entire volume of the sample. However, the measured density obtained from the approximate dimensions and weight is 4.45 g/cm^3 or 70% of the X-ray density of 6.36 g/cm^3 for stoichiometric $YBa_2Cu_3O_7$ using published lattice constants. Hence, the maximum superconducting volume is 70% of the plate due to the porosity of the sintered ceramic, while the shielding response suggests 97% is superconducting. This discrepancy is explained by the ability of the near surface shielding supercurrents to screen the interior of the plate. Low-field shielding data do not provide an accurate estimate of the superconducting fraction due to this screening effect which hides the interior porosity and any nonsuperconducting impurity phases as well. This fact dictates our preference for the Meissner fraction as indicated in section 2.3 despite the complications due to flux pinning.

Next, consider the nonlinear shielding response between 20 and 60 Oe in Figure 13. This is the field range where the transport critical current decreases by two orders of magnitude in typical ceramic $YBa_2Cu_3O_{7-\delta}$ (89-91), and the magnetization is reflecting grain decoupling in the plate. Although J_{ct} is small above 100 Oe in weakly linked material, the shielding can remain substantial due to **intragranular** supercurrents. The nonlinear region is the crossover from intergranular to intragranular screening. The volume susceptibility above 60 Oe in Figure 13 is $\chi_v = \chi_e = -0.69/4\pi$, where we have not used a demagnetization correction since the appropriate sample "shape" or effective dimensions are not determined in the decoupled grain regime. This problem has been solved for the ideal case of a spherical sample consisting of isotropic spherical decoupled grains close-packed on a cubic

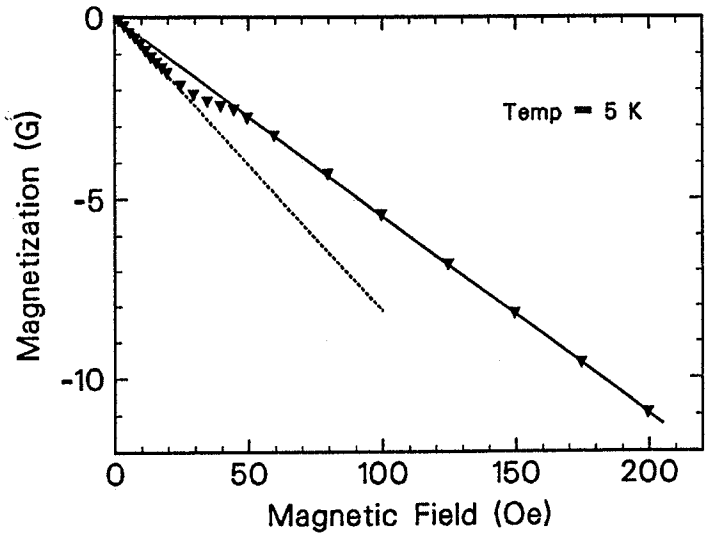

Figure 13: Shielding magnetization at 5 K versus external magnetic field for a thin plate cut from sintered superconducting $YBa_2Cu_3O_{7-\delta}$ ceramic. The dashed line indicates shielding of the entire volume by near surface supercurrents below 20 Oe. **Intergranular** supercurrents decrease rapidly above 20 Oe, resulting in essentially complete "grain decoupling" above 60 Oe. The solid line indicates **intragranular** shielding which dominates the magnetization at higher fields.

array (93). One way to test for grain decoupling is to measure the diamagnetic shielding for different orientations and look for demagnetization enhancements based on the shape of the entire sample. Full demagnetization corresponds to coupled grains, while little demagnetization implies decoupled grains (90).

Note that there is excellent agreement between the shielding fraction $-4\pi\chi_v = 0.69$ and the measured density of 70% of the x-ray density. We have found empirically that the mass susceptibility shielding fraction defined as $-4\pi\rho\chi_g$, where ρ is the x-ray density and χ_g is the mass susceptibility from Eq. 3, is nearly equal to one in a fully superconducting ceramic for fields above the grain decoupling field but below H_{c1}, independent of the porosity of the sample. The indication that grain decoupling has occurred is a magnetization response similar to that in Figure 13 where there are two well-defined linear regions. These two linear regions are not observed when the sample is ground to a powder such that the grains are always decoupled, and there is no obvious crossover from coupled to decoupled (intergranular to intragranular) shielding when the sample is almost completely dense such as hot-pressed ceramic. Mixed phase ceramics with grains which are decoupled at all fields show a nonlinear response even at the lowest fields, and the magnetization can be used to obtain an effective grain size if the penetration depth is known (26). Similar grain decoupling and low J_{ct} values in modest magnetic fields have been reported in ceramic samples of the newer Bi-Sr-Ca-Cu-O and Tl-Ca-Ba-Cu-O superconducting systems (62)(94).

Finally, consider the effect of grain decoupling on high-field magnetization hysteresis loops. The measured response is solely the intragranular mixed state behavior including shielding supercurrents and flux pinning. The critical current can be estimated using a modified Eq. 12 to accommodate the individual grain morphology and alignment, provided that "d" is the grain diameter rather than the bulk sample dimension. Note that an increase in hysteresis reflects better intragranular flux pinning, but it does **not** imply an improvement in the macroscopic intergranular critical current density. For example, neutron irradiation (95) or melting and quenching (96) have produced dramatic increases in hysteresis and thus J_{cm} for $YBa_2Cu_3O_{7-\delta}$ ceramic, but these data alone do not imply any improvement in J_{ct}.

A combination of DC magnetization, AC susceptibility, inductive and microstructural data can be used to determine an intrinsic J_{cm} value in ceramic material (39)(62)(90-92)(94)(97-99). An alternate approach is to disperse isolated grains from a ground superconducting powder in epoxy and induce grain alignment by applying a strong magnetic field while the epoxy hardens. If the grain morphology and relative concentration in the epoxy are known, magnetization hysteresis determines the anisotropic, intragranular J_{cm} (100)(101). These techniques yield values for intragranular J_{cm} in the 10^6-10^7 A/cm^2 range for high-temperature superconductors, and J_{ct} measurements on thin films confirm that these are realistic values.

One final point concerns the detection of impurity phases in ceramic samples. A substantial fraction of the common impurity phases contains isolated divalent paramagnetic Cu ions which have a Curie susceptibility given by Eqs. 4 and 5. Hence this contribution becomes strongest at low temperatures. Figure 4 shows that the low-field exclusion and expulsion in the superconducting phase(s) are temperature-independent at low temperatures, so the presence of a paramagnetic impurity phase(s) is detected by a diamagnetic exclusion or expulsion which becomes smaller in magnitude (less negative) as the temperature decreases. In particular, the Meissner signal can only increase as the temperature decreases (including flux creep, penetration depth, and H_{c1} considerations), so a decreasing Meissner signal at low temperature indicates that paramagnetic impurity phases are present. Shielding data are less reliable since surface screening currents can hide impurity phases in the interior of the sample. Impurity phases will also appear in high-field magnetization data: the superconducting diamagnetic response remains negative and decreases toward zero with increasing field in the mixed state (Figures 2 and 10), while a paramagnetic impurity phase will have a positive contribution that increases linearly with increasing field. Hence at sufficiently high field (but below H_{c2}), the impurity phase will become apparent as a linear field response in the magnetization data.

6.0 CONCLUDING REMARKS

Magnetization is a versatile and fundamental probe for superconducting materials, including the high-temperature copper-oxide-based superconductors. The normal state magnetic susceptibility contains information about both the electrical carriers and the copper spin system in the superconductor plus the behavior of any impurity phases present. The low-field magnetization in the superconducting state includes flux exclusion (diamagnetic shielding) and flux expulsion (Meissner effect) responses which differ due to flux pinning in single crystals and due to pinning, porosity, grain decoupling, and impurity phases in typical sintered ceramic material. Low-field data can be used to determine the fraction of superconducting material and the lower critical field H_{c1}. High-field data are used to study flux pinning and magnetization hysteresis which can be related to the critical current density versus field and temperature. Weak pinning and the associated "giant flux creep" are major concerns in high-temperature superconductors, and magnetization relaxation directly addresses this phenomenon. Two substantial challenges for application of these materials are to increase flux pinning and to improve intergranular supercurrents in ceramic samples. Magnetization measurements are essential in assessing progress on these challenges.

ACKNOWLEDGEMENTS

This work was performed at Sandia National Laboratories, supported by the U. S. Department of Energy under Contract No. DE-AC04-76DP00789. Several conspirators in high-temperature superconductivity have provided materials and ideas including T. L. Aselage, R. J. Baughman, D. S. Ginley, J. F. Kwak, B. Morosin, J. E. Schirber, and C. P. Tigges.

7.0 REFERENCES

1. W. Meissner and R. Ochsenfeld, *Naturwissen*, 21:787 (1933).
2. D. Shoenberg, *Superconductivity*, Cambridge Univ. Press, London, Ch. 6 (1952).
3. P.G. De Gennes, *Superconductivity of Metals and Alloys*, translated by P.A. Pincus, W.A. Benjamin, New York, Ch. 5 (1966).
4. D. Saint-James, G. Sarma and E.J. Thomas, *Type II Superconductivity*, Pergamon, Oxford, p. 4 (1969).
5. D. Saint-James, G. Sarma and E.J. Thomas, *ibid.*, Ch. 1, 3, 8.
6. M. Tinkham, *Introduction to Superconductivity*, McGraw-Hill, New York, Ch. 1, 3, 5.(1975).
7. A.C. Rose-Innes and E. H. Roderick, *Introduction to Superconductivity*, 2nd ed., Pergamon, Oxford, Ch. 2, 4, 6, 12, (1978).
8. J.H. Van Vleck, *The Theory of Electric and Magnetic Susceptibilities*, Oxford, London, p. 233, (1932).
9. Landolt-Bornstein, New Series, Group II: Atomic and Molecular Physics, Vol. 2, *Magnetic Properties of Coordination and Organo-Metallic Compounds*, ed. by E. Konig, Springer-Verlag, Berlin, pp. 1-1 to 1-25, (1966).
10. H.J. Zeiger and G.W. Pratt, *Magnetic Interactions in Solids* Oxford, London, pp. 405-408, (1973).
11. A.A. Abrikosov, *Fundamentals of the Theory of Metals*, North-Holland, New York, p. 173-178, (1988).
12. G. Shirane, Y. Endoh, R.J. Birgeneau, M.A. Kastner, Y. Hidaak, M. Oda, M. Suzuki, T. Murakami, *Phys. Rev. Lett.* 59:1613 (1987).
13. J.M. Tranquada, D.E. Cox, W. Kunnmann, H. Moudden, G. Shirane, M. Suenaga, P. Zolliker, D. Vaknin, S.K. Sinha, M.S. Alvarez, A.J. Jacobson, D.C. Johnston, *Phys. Rev. Lett.* 60:156 (1988).

14. R.J. Birgeneau, D.R. Gabbe, H.P. Jenssen, M.A. Kastner, P.J. Picone, T.R. Thurston, G. Shirane, Y. Endoh, M. Sato, K. Yamada, Y. Hidaka, M. Oda, Y. Enomoto, M. Suzuki, T. Murakami, *Phys. Rev.* B 38:6614 (1988).
15. H. Takagi, T. Ido, S. Ishibashi, M. Uota, S. Uchida, Y. Tokura, *Phys. Rev.* B 40:2254 (1989) and references therein.
16. Y. Yamaguchi, M. Tokumoto, S. Waki, Y. Nakagawa, Y. Kimura, *J. Phys. Soc. Japan* 58:2256 (1989) and references therein.
17. D.C. Johnston, *Phys. Rev. Lett.* 62:957 (1989).
18. J.A.O. de Aguiar, A.A. Menovsky, J. van der Berg, H.B. Brom, *J. Phys.* C 21:L237 (1988).
19. S. Tyagi, M. Barsoum, K.V. Rao, *Phys. Lett.* A 128:225 (1988).
20. F. Mehran, S.E. Barnes, T.R. McGuire, T.R. Dinger, D. Kaiser, F. Holtzberg, *Solid State Commun.* 66:299 (1988).
21. E.A. Lynton, *Superconductivity*, Metheun, London, p. 23 (1969). Actually, all three fields (B, H_i, and M) are zero in the interior, but it is convenient to treat the superconductor as if it were a magnetic body where M is the equivalent magnetization produced by the screening supercurrents.
22. A.M. Campbell and J.E. Evetts, *Critical Currents in Superconductors*, Taylor and Francis, London, p. 3, (1972).
23. L. Krusin-Elbaum, R.L. Greene, F. Holtzberg, A.P. Malozemoff, Y. Yeshurun, *Phys. Rev. Lett.* 62:217 (1989).
24. D. Shoenberg, *op. cit.*, p. 143 and 197.
25. D. Shoenberg, *ibid.*, p. 165.
26. D.E. Farrell, M.R. DeGuire, B.S. Chandrasekhar, S.A. Alterovitz, P.R. Aron, R.L. Fagaly, *Phys. Rev.* B 35:8797 (1987) and references therein.
27. J.A. Osborn, *Phys. Rev.* 67:351 (1945).
28. E.C. Stoner, *Phil. Mag.* 36:803 (1945).

29. A.H. Morrish, *The Physical Principles of Magnetism*, pp. 8-11, Wiley, New York, (1965).

30. S. Chikazumi and S.H. Charap, *Physics of Magnetism*, Wiley, New York, pp. 19-24 (1964).

31. E.L. Venturini, J.F. Kwak, D.S. Ginley, R.J. Baughman, B. Morosin, *Physica* C 162-164: 673 (1989).

32. Y. Yeshurun, A.P. Malozemoff, F. Holtzberg, T.R. Dinger, *Phys. Rev.* B 38:11828 (1988).

33. A. Umezawa, G.W. Crabtree, J.Z. Liu, T.J. Moran, S.K. Malik, L.H. Nunez, W.L. Kwok, C.H. Sowers, *Phys. Rev.* B 38:2843 (1988).

34. L. Krusin-Elbaum, A.P. Malozemoff, Y. Yeshurun, D.C. Cronemeyer, F. Holtzberg, *Phys. Rev.* B 39:2936 (1989).

35. A.P. Malozemoff, "Macroscopic Magnetic Properties of High Temperature Superconductors", in *Physical Properties of High Temperature Superconductors I*, ed. by D. M. Ginsberg, World Scientific, Singapore, Ch. 3, and references therein (1989).

36. L. Schimmele, H. Kronmuller, H. Teichler, *Phys. Stat. Solid* (b) 147:361 (1988).

37. A.P. Malozemoff, L. Krusin-Elbaum, D.C. Cronemeyer, Y. Yeshurun, F. Holtzberg, *Phys. Rev.* B 38:6490 (1988).

38. D.S. Ginley, E.L. Venturini, J.F. Kwak, R.J. Baughman, B. Morosin, J.E. Schirber, *Phys. Rev.* B 36:829 (1987).

39. R.L. Peterson, *Phys. Rev.* B 40:2678 (1989).

40. L. Krusin-Elbaum, A.P. Malozemoff, Y. Yeshurun, D.C. Cronemeyer, F. Holtzberg, *Physica* C 153-155:1469 (1988).

41. W.J. Carr, Jr., *AC Loss and Macroscopic Theory of Superconductors*, Gordon and Breach, New York, Ch. 4, (1983).

42. C.P. Bean, *Phys. Rev. Lett.* 8:250 (1962).

43. H. London, *Phys. Lett.* 6:162 (1963).

44. Y.B. Kim, C.F. Hempstead, A.R. Strnad, *Phys. Rev.* 129:528 (1963).

45. C.P. Bean, *Rev. Mod. Phys.* 36:31 (1964).

46. W.A. Fietz and W.W. Webb, *Phys. Rev.* 178:657 (1969).

47. A.M. Campbell and J.E. Evetts, *op. cit.*, pp. 45-81.

48. E.M. Gyorgy, R.B. van Dover, K.A. Jackson, L.F. Schneemeyer, J.V. Waszczak, *Appl. Phys. Lett.* 55:283 (1989).

49. T.R. Dinger, T.K. Worthington, W.J. Gallagher, R.L. Sandstrom, *Phys. Rev. Lett.* 58:2687 (1987).

50. G.W. Crabtree, J.Z. Liu, A. Umezawa, W.K. Kwok, C.H. Sowers, S.K. Malik, B.W. Veal, D.J. Lam, M.B. Brodsky, J.W. Downey, *Phys. Rev.* B 36:4021 (1987).

51. R.L. Fleischer, H.R. Hart, Jr., K.W. Lay, F.E. Luborsky, *Phys. Rev.* B 40:2163 (1989).

52. A.P. Malozemoff, T.K. Worthington, Y. Yeshurun, F. Holtzberg, P.H. Kes, *Phys. Rev.* B 38:7203 (1988).

53. P. Chaddah, K.V. Bhagwat, G. Ravikumar, *Physica* C 159:570 (1989).

54. Y. Yeshurun and A.P. Malozemoff, *Phys. Rev. Lett.* 60:2202 (1988).

55. D.E. Farrell, B.S. Chandrasekhar, M.R. DeGuire, M.M. Fang, V.G. Kogan, J.R. Clem, D.K. Finnemore, *Phys. Rev.* B 36:4025 (1987).

56. R.N. Shelton, R.W. McCallum, M.A. Damento, K. Gschneider, Jr., *Intern. J. Mod. Phys.* B 1:401 (1988).

57. G.M. Stollman, B. Dam, J.H.P.M. Emmen, J. Pankert, *Physica* C 159:854 (1989).

58. R.B. van Dover, L.F. Schneemeyer, E.M. Gyorgy, J.V. Waszczak, *Appl. Phys. Lett.* 52:1910 (1988).

59. J. van den Berg, C.J. van der Beek, P.H. Kes, J.A. Mydosh, M.J.V. Menken, A.A. Menovsky, *Supercond. Sci. Techn.* 1:249 (1989).

60. H. Kumakura, K. Togano, E. Yanagisawa, H. Maeda, *Appl. Phys. Lett.* 55:185 (1989).

61. J.F. Kwak, E.L. Venturini, R.J. Baughman, B. Morosin, D.S. Ginley, *Cyrogenics* 29:291 (1989).

62. J.R. Thompson, J. Brynestad, D.M. Kroeger, Y.C. Kim, S.T. Sekula, D.K. Christen, E.D. Specht, *Phys. Rev.* B 39:6652 (1989).

63. A.P. Malozemoff, T.K. Worthington, R.M. Yandrofski, Y. Yeshurun, *Intern. J. Mod. Phys.* B 1:1293 (1988).

64. E.M. Gyorgy, R.B. van Dover, S. Jin, R.C. Sherwood, L.F. Schneemeyer, T.H. Tiefel, J.V. Waszczak, *Appl. Phys. Lett.* 53:2223 (1988).

65. E.L. Venturini, J.F. Kwak, D.S. Ginley, B. Morosin, R.J. Baughman in *Science and Technology of Thin Film Superconductors*, ed. by R.D. McConnell and S.A. Wolf, Plenum, New York, p. 395, (1989).

66. B. Placais, P. Mathieu, Y. Simon, *Solid State Commun.* 71:177 (1989).

67. U. Dai, N. Hess, L.R. Tessler, G. Deutscher, G. Vetter, F. Queyroux, N. Bontemps, R. Mahoum, M. Lagues, P. Mocaer, *Appl. Phys. Lett.* 55:1135 (1989).

68. T.R. McGuire, D. Dimos, R.H. Koch, R.B. Laibowitz, J. Mannhart, *IEEE Trans. Magnetics* 25:3218 (1989).

69. Y.B. Kim, C.F. Hempstead, A.R. Strnad, *Phys. Rev. Lett.* 9:306 (1962).

70. P.W. Anderson, *Phys. Rev. Lett.* 9:309 (1962).

71. Y.B. Kim, C.F. Hempstead, A.R. Strnad, *Phys. Rev.* 131:2486 (1963).

72. P.W. Anderson and Y.B. Kim, *Rev. Mod. Phys.* 36:39 (1964).

73. M.R. Beasley, R. Labusch, W.W. Webb, *Phys. Rev.* 181:682 (1969).

74. Y.B. Kim and M.J. Stephen in *Superconductivity*, Vol. 2, ed. by R.D. Parks, Marcel Dekker, New York, Ch. 19, (1969).

75. K.A. Muller, M. Takashige, J.G. Bednorz, *Phys. Rev. Lett.* 58:1143 (1987).

76. A.C. Mota, A. Pollini, P. Visani, K.A. Muller, J.G. Bednorz, *Phys. Rev.* B 36:4011 (1987).

77. C. Giovannella, G. Collin, P. Rouault and I.A. Campbell, *Europhys. Lett.* 4:109 (1987).

78. I. Morgenstern, K.A. Muller, J.G. Bednorz, *Z. Phys.* B 69:33 (1987).

79. M. Tinkham, *op. cit.*, Ch. 5.

80. Y. Yeshurun, A.P. Malozemoff, F. Holtzberg, *J. Appl. Phys.* 64:5797 (1988).

81. Y. Yeshurun, A.P. Malozemoff, T.K. Worthington, R.M. Yandrofski, L. Krusin-Elbaum, F.H. Holtzberg, T.R. Dinger, G.V. Chandrashekhar, *Cryogenics* 29:258 (1989).

82. P.H. Kes, J. Aarts, J. van den Berg, C.J. van der Beek, J.A. Mydosh, *Supercond. Sci. Techn.* 1:242 (1989).

83. M.E. McHenry, M.P. Maley, E.L. Venturini and D.S. Ginley, *Phys. Rev.* B 39:4784 (1989).

84. C.W. Hagen, R.P. Griessen, E. Salomons, *Physica* C 157:199 (1989).

85. K. Yamafuji, T. Fujiyoshi, K. Toko, T. Matsushita, *Physica* C 159:743 (1989).

86. H.S. Lessure, S. Simizu, S.G. Sankar, *Phys. Rev.* B 40:5165 (1989).

87. J.G. Bednorz and K.A. Muller, *Z. Phys.* B 64:189 (1986).

88. M.K Wu, J.R. Ashburn, C.J. Torng, P.H. Hor, R.L. Meng, L. Gao, Z.J. Huang, Y.Q. Wang, C.W. Chu, *Phys. Rev. Lett.* 58:908 (1987).

89. J.W. Ekin, A.I. Braginski, A.J. Panson, M.A. Janocko, D.W. Capone II, N.J. Zaluzec, B. Flandermeyer, O.F. de Lima, M. Hong, J. Kwo, S.H. Liou, *J. Appl. Phys.* 62:4821 (1987) and references therein.

90. J.F. Kwak, E.L. Venturini, D.S. Ginley, W. Fu, in *Novel Superconductivity*, ed. by S.A. Wolf and V.Z. Kresin Plenum, New York, p. 983, (1987).

91. D.C. Larbalestier, M. Daeumling, X. Cai, J. Seuntjens, J. McKinnell, D. Hampshire, P. Lee, C. Meingast, T. Willis, H. Muller, R.D. Ray, R.G. Dillenburg, E.E. Hellstrom, R. Joynt, *J. Appl. Phys.* 62:3308 (1987).

92. J.R. Clem, *Physica* C 153-155:50 (1988).

93. J.R. Clem and V.G. Kogan, *Japan J. Appl. Phys.* 26: Suppl. 26-3 (Proc. 18th Intern. Conf. Low Temp. Phys.), p. 1161 (1987).

94. H. Kupfer, S.M. Green, C. Jiang, Yu Mei, H.L. Luo, R. Meier-Hirmer, C. Politis, *Z. Phys.* B 71:63 (1988).

95. J.R. Cost, J.O. Willis, J.D. Thompson, D.E. Peterson, *Phys. Rev.* B 37:1563 (1988).

96. M. Murakami, M. Morita, N. Koyama, *Japan J. Appl. Phys.* 28:L1125 (1989).

97. H. Kupfer, I. Apfelstedt, W. Schauer, R. Flukiger, R. Meier-Hirmer, H. Wuhl, *Z. Phys.* B 69:159 (1987).

98. D.C. Larbalestier, S.E. Babcock, X. Cai, M. Daeumling, D.P. Hampshire, T.F. Kelly, L.A. Lavanier, P.J. Lee, J. Seuntjens, *Physica* C 153-155:1580 (1988).

99. E. Babic, D. Drobac, J. Horvat, Z. Marohnic, M. Prester, *Supercond. Sci. Technol.* 2:164 (1989).

100. M.M. Fang, V.G. Kogan, D.K. Finnemore, J.R. Clem, L.S. Chumbley, D.E. Farrell, *Phys. Rev.* B 37:2334 (1988).

101. M.M. Fang, D.K. Finnemore, D.E. Farrell, N.R. Bansal, *Cryogenics* 29:347 (1989).

Part IV

Structure-Property Considerations